Check for updates

RESEARCH ARTICLE

NANO · MICRO small
www.small-journal.com

SERS Sensor Integrated in Stretchable and Antimicrobial Wrapper for Food Quality Monitoring and Preservation

Ji-Hwan Ha, Jinhyeok Yang, Dodam Kim, Wonjoon Lee, Channyeong Yun, Soon Hyoung Hwang, Sohee Jeon, Jungrak Choi, Hakhyun Lim, Minki Kim, Dahong Kim, Su A Park, Junhyuk Choi, Joong-Won Song, Sunae So, Junseong Ahn,* and Jun-Ho Jeong**

In the wellness era, where food quality and safety are paramount, traditional food-monitoring methods, such as ribotyping and polymerase chain reaction, are often destructive and time-consuming, limiting their practicality for widespread application. Surface-enhanced Raman scattering (SERS) sensing is a promising alternative that offers real-time, nondestructive, and highly sensitive capabilities. This study proposes a nanostructured SERS sensor integrated into a stretchable and antimicrobial wrapper (NSSAW). The system, which is fabricated using nanoimprint lithography, nanotransfer printing, and electrospinning, incorporates an Au nanostructure array loaded with Ag nanoparticles, creating numerous SERS hotspots. The electrospun wrapper, composed of composite nanofibers infused with curcumin, provides enhanced elasticity and antimicrobial properties. NSSAW facilitates on-site, non-destructive detection of nutritional content, freshness, and toxicants in food, while preventing microbial growth and enhancing preservation. The effectiveness of NSSAW is demonstrated by detecting purines, proteins, and lipids in salmon, textured vegetable protein (TVP), beef, and pork, as well as carotenoids and thiram in oranges. Furthermore, NSSAW effectively monitors and delays spoilage progression over time, as evidenced by the monitoring of bacterial emissions. NSSAW aims to replace conventional food packaging materials, enabling smart food monitoring and preservation, and ultimately contributing to improved food safety and quality in the wellness era.

1. Introduction

Interest in food, one of the most essential elements for human survival, has steadily grown since the dawn of humanity. In the current wellness era, characterized by an increased focus on healthcare, people are not only concerned with the quantity and taste of their food but also with its quality and safety. For example, high-quality foods, such as protein-rich meats and pesticide-free fruits, are valued significantly higher in the market compared to their lower-quality counterparts.[1–3] Consequently, monitoring the nutritional content, freshness, and toxicants in these foods has become critically important.[4]

To address this need, various methods for food monitoring have been developed, including molecular biology, ribotyping, enzyme-linked immunosorbent assay, flow cytometry, and polymerase chain reaction.[5,6] However, most of these methods rely on destructive sampling and require 2–12 h to produce results, making them impractical for general or

J.-H. Ha
Department of Mechanical Engineering
Hanbat National University
Daejeon 34158, Republic of Korea

J. Yang, D. Kim, H. Lim, M. Kim, J.-W. Song
Department of Electro-Mechanical Systems Engineering
Korea University
Sejong 30019, Republic of Korea

W. Lee
Zorvex
Suwon 16229, Republic of Korea

C. Yun
Trackfarm
Asan 31470, Republic of Korea

S. H. Hwang, S. Jeon, D. Kim, S. A Park, J. Choi, J.-H. Jeong
Nano Lithography and Manufacturing Research Center
Korea Institute of Machinery and Materials (KIMM)
Daejeon 34103, Republic of Korea
E-mail: jhjeong@kimm.re.kr

J. Choi
Electronics and Telecommunications Research Institute (ETRI)
Daejeon 34129, Republic of Korea

S. So, J. Ahn
Department of Control and Instrumentation Engineering
Korea University
Sejong 30019, Republic of Korea
E-mail: sunaeso@korea.ac.kr; junseong@korea.ac.kr

The ORCID identification number(s) for the author(s) of this article can be found under https://doi.org/10.1002/smll.202501808

DOI: 10.1002/smll.202501808

 © 2025 Wiley-VCH GmbH

commercial use.[7] In this context, surface-enhanced Raman scattering (SERS) sensing offers a promising solution. SERS is considered a next-generation food-monitoring method because of its ability to detect unknown target molecules on-site in real-time with non-destructive, high-sensitivity, and high-specificity characteristics. Over the past decade, several studies have confirmed the effectiveness of SERS in accurately monitoring food quality, including the detection of proteins in fish and meat and assessing the freshness of fruits.[8,9] Furthermore, SERS has been employed in food safety monitoring by detecting contaminants, such as norfloxacin and melamine in milk, as well as chlorpyrifos and thiabendazole in fruits. It has also demonstrated the capability to simultaneously detect other harmful substances, including foodborne viruses and bacterial toxins.[10,11] However, these early studies have primarily focused on the feasibility of using SERS for food quality and safety monitoring, rather than its practical applications.

Current SERS platforms are typically designed in liquid or rigid forms, requiring separate preparation and food sampling.[12–18] This process involves cutting a piece of food and placing it on the SERS platform, which undermines the non-destructive advantage of SERS and limits its accessibility and practicality. Additionally, conventional SERS sensors for food monitoring are typically limited to detecting only one or two specific nutrients or elements and cannot analyze multiple components simultaneously. Furthermore, they do not incorporate strategies to enhance long-term food preservation, thereby limiting their overall functionality in food quality management.

To address these limitations, we propose an innovative approach: a nanostructured SERS sensor integrated into a stretchable and antimicrobial wrapper (NSSAW). Nanostructured SERS sensors enable real-time, on-site, and non-destructive detection of nutritional content, freshness, and toxicants in food. Stretchable and antimicrobial wrappers provide damage-free packaging and prevent microbial growth, thereby enhancing the preservation duration and conditions. The sensor component consists of an Au nanostructure array loaded with Ag nanoparticles (NPs), which creates a SERS platform with numerous hotspots. The Au nanostructure, fabricated via nanoimprint lithography (NIL) and e-beam slanted deposition, serves as a stable substrate for Ag NPs and exhibits gas permeability. The Ag NPs significantly enhance the Raman signal (30.11 times in experiments) through localized surface plasmon resonances, as designed and verified by finite-difference time-domain (FDTD) numerical simulations. The food quality and safety monitoring capability of NSSAW was demonstrated by detecting purines, proteins, and lipids in salmon, TVP, beef, and pork, as well as carotenoids and thiram in oranges.

The wrapper component was directly electrospun over the Au-Ag nanostructured SERS sensor, with the nanostructure spontaneously integrated into the electrospun wrapper via nanotransfer printing (nTP). The wrapper, made of thermoplastic polyurethane (TPU), has excellent elasticity. Additionally, the wrapper incorporated a natural antimicrobial agent, curcumin, which exhibited high antimicrobial activity against *S. aureus* (99.99%) and *E. coli* (99.9%). Finally, we demonstrated that the sensor component of NSSAW not only monitors the nutritional content of food but also tracks the progression of spoilage over time by detecting the dimethyl disulfide (DMDS) peak released by bacteria, whereas the wrapper effectively delayed microbial growth. By analyzing the composition, freshness, and toxicants of each food item in real-time, NSSAW supports more effective food management and consumption.

2. Results

2.1. Overall Research Concept

Figure 1 illustrates the comprehensive strategy and application of the developed NSSAW for food protection and monitoring. Figure 1a presents a detailed depiction of the research concept. The NSSAW was fabricated using an electrospinning process to produce two types of fibers: TPU-based and curcumin-TPU (C-TPU) fibers, each tailored for distinct functionalities, that is, food monitoring and preservation, respectively. TPU-based fibers were functionalized with Au nanostructures, which were transferred onto the fibers to create plasmonic hotspots. Additionally, Ag NPs are drop-cast onto the Au-coated fibers, which embeds the Ag NPs within the Au nanostructure. This configuration significantly enhances electromagnetic hotspots, enabling SERS for noninvasive and nondestructive analysis of food freshness and composition. In parallel, the electrospun C-TPU fibers leveraged the antimicrobial properties of curcumin, which is rich in polyphenols. These fibers effectively inhibit the growth and reproduction of microorganisms, reduce spoilage of meat and fish, extend their shelf life, and potentially mitigate pest infestations during the growth and harvesting stages of fruit production.

Figure 1b shows the applications of versatile electrospun fiber-based NSSAW for food preservation and monitoring. The images illustrate the food-monitoring patches applied to i) oranges, ii) beef, and iii) sushi. For oranges, the NSSAW was layered to demonstrate its ability to support growth while preserving freshness. In the cases of beef and sushi, the NSSAW enabled real-time monitoring of food freshness and composition, ensuring quality up to the point of consumption. A notable feature of the NSSAW is its integration with SERS technology, which allows the monitoring patch to function as a barcode for microscopic food analysis directly on the food surface. This capability facilitates immediate assessment of food freshness and reduces the risk of foodborne illnesses. Moreover, it has significant potential for dietary management in modern lifestyles. This would benefit individuals with specific nutritional needs, such as those requiring strict dietary control.

2.2. Fabrication and Morphological Analysis of NSSAW

Figure 2 highlights the fabrication strategies and morphological characteristics of the NSSAW. To transfer the Au nanostructure array onto the C-TPU electrospun fibers, three strategies were employed: Au slanted deposition, plasma surface modification, and lateral etching of the polyurethane acrylate (PUA) nanoarray mold. As shown in Figure 2a, (i) the nanopattern mold was initially fabricated using a UV-curable PUA resin via NIL with a nanostructured silicon master mold. (ii) After replicating the nanoarray, a 100 nm-thick layer of Au was deposited onto the PUA surface with nanofiller structures using e-beam evaporation. During this deposition process, the target substrate (the

© 2025 Wiley-VCH GmbH

16136829, 2025, 38, Downloaded from https://onlinelibrary.wiley.com/doi/10.1002/smll.202501808 by Korea University Library, Wiley Online Library on [28/09/2025]. See the Terms and Conditions (https://onlinelibrary.wiley.com/terms-and-conditions) on Wiley Online Library for rules of use; OA articles are governed by the applicable Creative Commons License

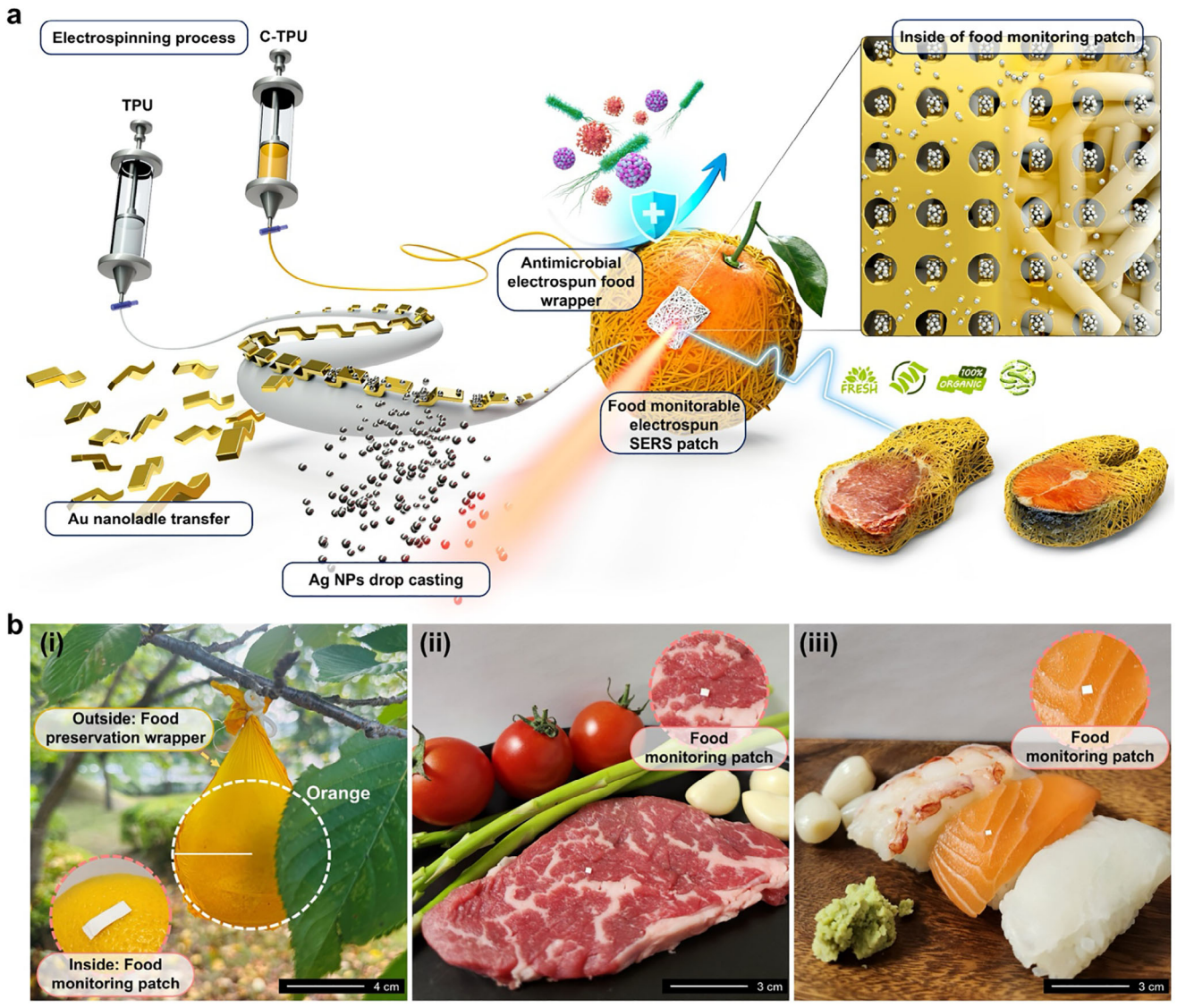


Figure 1. Strategy for fabrication and practical application of nanostructured SERS sensors integrated into a stretchable and antimicrobial wrapper (NSSAW) for food monitoring and preservation. a) Schematic of the NSSAW fabrication and functionalization strategies for food monitoring and preservation. b) Practical applications of NSSAW for food preservation and monitoring of various food types. i) Integration into the peel of an orange to monitor growth while maintaining freshness. ii) Application to beef for real-time monitoring of freshness and composition. iii) Application in sushi to ensure quality and safety up to the consumption point.

nanostructured PUA mold) was tilted at an angle of 30° from the direction of Au deposition to induce a ladle shape, with one side connected to a disk on top of a pillar structure. Consequently, the Au nanostructure is formed on one side, while the other side remains undeposited, exposing the PUA surface. (iii) To reliably transfer the Au nanostructure onto the electrospun wrapper, oxygen plasma treatment proves highly effective.[19–21] This treatment enhances surface energy, facilitating adhesion between the Au nanostructure array and the electrospun fibers, while reducing adhesion between the Au nanostructure array and the PUA by selectively etching the exposed surface of the polymer. (iv) The Au nanostructure array mold, subjected to oxygen plasma etching, is then prepared for C-TPU electrospinning, which acts as a stretchable and antimicrobial wrapper. Electrospun fibers were precisely laminated onto the prepared nanoarray surface. The reduced adhesion between the Au nanostructure array and the PUA mold, combined with the enhanced adhesion driven by electrostatic attraction during electrospinning, facilitates the seamless transfer of the Au nanostructure array onto the electrospun wrapper substrate without the need for heat or pressure. (v) Finally, Ag NPs were meticulously drop-cast onto the Au nanostructure and integrated to amplify the SERS sensing signal.

The electrospinning process employed for antimicrobial packaging is a well-established technique for producing microscale to nanoscale fibers.[22,23] Scanning electron microscopy (SEM) analysis indicated that the fabricated C-TPU exhibited a random orientation, revealing the presence of numerous microscale pores between the fibers, as shown in Figure 2b. Figure 2c shows that a

© 2025 Wiley-VCH GmbH

16136829, 2025, 38, Downloaded from https://onlinelibrary.wiley.com/doi/10.1002/smll.202501808 by Korea University Library, Wiley Online Library on [28/09/2025]. See the Terms and Conditions (https://onlinelibrary.wiley.com/terms-and-conditions) on Wiley Online Library for rules of use; OA articles are governed by the applicable Creative Commons License

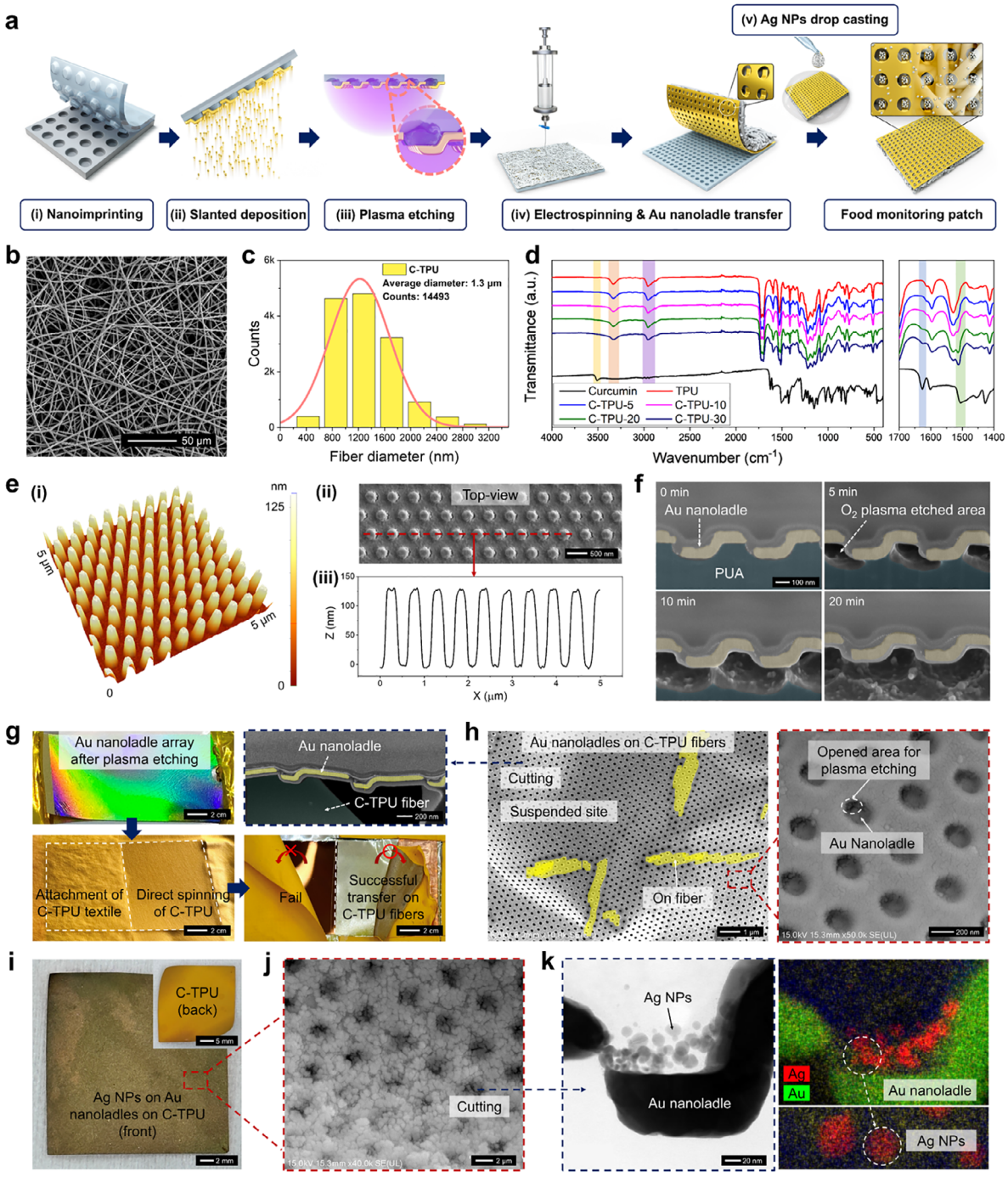


Figure 2. Fabrication details and morphological analysis of the electrospun C-TPU wrapper incorporating the Au nanostructure array with Ag NPs. a) Schematic of the NSSAW fabrication process: i) Fabrication of the nanopatterned PUA mold via NIL, followed by (ii) slanted Au deposition to form the Au nanostructures. iii) Oxygen plasma treatment to enhance adhesion between the Au nanoarray and electrospun fibers while reducing adhesion to the PUA mold. iv) Electrospinning C-TPU fibers onto the prepared nanoarray surface, enabling the seamless transfer of the Au nanostructures without the application of heat or pressure. v) Drop-casting Ag NPs onto the Au nanostructures. b) SEM images of the electrospun C-TPU wrapper (top view). c) Fiber distribution within the electrospun C-TPU wrapper. d) FTIR analysis of curcumin, TPU, and C-TPU (with curcumin contents of 5, 10, 20, and 30 wt.%). e) AFM 3D depth analysis revealing a nanocolumnar structure: i) A total of 100 nanopatterned columns distributed over an area of 5 μm × 5 μm, ii) a top-view SEM image, and iii) a uniform height of 125 nm confirmed through the z-axis profile. f) Cross-sectional FIB-SEM images of PUA-based nanostructured molds at varying oxygen plasma treatment times. g) Photograph showing the result of spinning an electrospun wrapper directly onto the Au nanostructure array surface, with SEM confirmation of the successful transfer of the Au nanostructures onto the electrospun fiber surface. h) Top-view SEM image of the Au nanostructure array transferred onto the fiber surface of the electrospun wrapper, showing open areas in the pattern due to oblique deposition. i) Photograph taken after drop-casting Ag NPs. j) SEM analysis showing the even distribution of Ag NPs on the surface and within the Au nanostructure array. k) NSSAW FIB-TEM cross-sectional analysis and EDS elemental analysis results.

© 2025 Wiley-VCH GmbH

16136829, 2025, 38, Downloaded from https://onlinelibrary.wiley.com/doi/10.1002/smll.202501808 by Korea University Library, Wiley Online Library on [28/09/2025]. See the Terms and Conditions (https://onlinelibrary.wiley.com/terms-and-conditions) on Wiley Online Library for rules of use; OA articles are governed by the applicable Creative Commons License

single fiber strand of this functional wrapper, characterized by its random weave, has an average diameter of ≈1.3 µm (with a standard deviation of 0.22 µm). A morphological assessment of 14493 fibers confirmed a predominantly distributed diameter range of 800–1500 nm. Fourier-transform infrared (FTIR) analysis confirmed that the fibers were a composite of curcumin, known for its potent antibacterial properties, and TPU, which is renowned for its excellent elasticity. Notably, characteristic absorption peaks corresponding to hydroxyl groups (3500–3600 cm^{-1}) and carbonyl groups (1600–1700 cm^{-1}) from curcumin, as well as urethane groups (3300–3400 cm^{-1}; 1500–1550 cm^{-1}) from TPU, were observed (Figure 2d). Additionally, an increase in the intensity of hydroxyl and carbonyl groups was detected as the curcumin content increased to 5, 10, 20, and 30 wt.%, further corroborating the composite properties of C-TPU.

The fabrication of nanostructured Au via NIL and the effects of subsequent oxygen plasma treatments are introduced. Figure 2e presents the 3D depth profiles of the initial nanocolumnar structures obtained using atomic force microscopy (AFM). Specifically, (i) 100 nanopillar structures were designed within a 5 × 5 μm^2 area, with heights measured up to 125 nm; (ii) SEM top-view imaging substantiated the formation of a uniform columnar architecture with a consistent height of 125 nm; and (iii) the z-axis profile confirmed the homogeneity of the height of the structures at 125 nm. Au was deposited at an inclination angle of 30° onto the nanopillar structures using a slanted deposition method, followed by oxygen plasma treatment. Figure 2f shows the progressive etching of the PUA mold as a function of the oxygen plasma treatment duration, verified through cross-sectional views obtained by FIB-SEM analysis. Increasing the oxygen plasma treatment times to 5, 10, and 20 min resulted in substantial etching of the PUA nanostructure area, reducing the interface contact with the Au nanostructures. After etching, C-TPU electrospinning was performed on the Au nanostructure surfaces. The electrospinning apparatus used for C-TPU fiber fabrication is described in Supplementary Figure S1 (Supporting Information). The Au nanostructure array was grounded to facilitate adhesion between the C-TPU and Au nanostructures via electrostatic interactions. Consequently, the Au nanostructures were successfully transferred onto the electrospun wrapper without the application of heat or pressure during the process.

For comparison, an additional test was conducted for both scenarios. In the first scenario, a separately fabricated electrospun C-TPU wrapper was attached to the Au nanostructures. In the second scenario, C-TPU was electrospun directly onto the Au nanostructures, whereas in the first scenario, the separately fabricated wrapper did not transfer the Au nanostructure array through contact. However, in the second scenario, the direct electrospinning process enabled the transfer of the Au structures via electrostatic attraction, as shown in Figure 2g. This demonstrates that the transfer method relies on the potential difference between the Au nanostructure array (grounded) and charged electrospun wrapper (positively charged). Figure 2h illustrates the morphology of the Au nanostructures transferred onto the electrospun C-TPU fibers, as observed by SEM analysis. The Au nanostructures, with a diameter of 200 nm and a pitch of 550 nm, exhibited no physical damage, such as cracks or deformations, because they were not subjected to heat or pressure during the transfer process.

To further enhance the SERS hotspots, Ag NPs were embedded in the Au nanostructure array. A solution of Ag NPs, dispersed in a liquid phase with a diameter of 20 nm, was carefully drop-cast to ensure compatibility with the gap size between the Au nanostructures. As shown in Figure 2i, the Ag NPs were successfully integrated into the Au nanostructure array on the electrospun C-TPU wrapper. The front side of the wrapper exhibits a gray-gold hue due to the combined presence of the Au nanostructures and Ag NPs, whereas the back side displays a dark yellow color, attributed to curcumin derived from turmeric.

Figure 2j presents the surface morphology analyzed by SEM. The SEM image revealed a uniformly coated surface of the functionalized wrapper, with Ag NPs arranged within the Au nanostructure array. Additionally, the transmission electron microscopy (TEM) analysis, as shown in Figure 2k, provides cross-sectional views of the Au nanostructures and Ag NPs. The gaps within the nanostructure array, ≈20 nm wide, resulted from the 30° slanted deposition of a 100 nm-thick Au layer. These narrow gaps effectively accommodate 20 nm diameter Ag NPs, ensuring secure integration without displacement. EDS mapping analysis further confirmed that the Ag NPs were evenly distributed throughout the Au nanostructure.

2.3. Characterization of NSSAW for Food Quality Preservation

When using a wrapper to preserve the freshness of foods, such as fruit, fish, and meat, key factors such as robust mechanical strength, high stretchability, non-toxicity, and antimicrobial effectiveness must be considered. **Figure 3** presents an evaluation of the specialized properties of the electrospun C-TPU wrapper incorporating an Au nanostructure array with Ag NPs. Figure 3a illustrates the mechanical properties of electrospun C-TPU. The sample exhibited exceptional elongation at break, reaching 716%, with a maximum stress of 52.3 MPa. The Young's modulus was calculated as 0.105 MPa. This remarkable mechanical stretchability makes electrospun C-TPU an ideal material for conformally wrapping foods with various shapes, offering effective protection against physical damage.

To ensure that the electrospun wrapper was non-toxic when in contact with food, cell growth tests were conducted, and SEM analysis was performed to observe cell morphology on Days 4 and 7. Both pure TPU and C-TPU electrospun wrappers demonstrated stable cell growth (indicated in blue), with the C-TPU fibers showing superior cell growth rates. This enhanced cell growth was attributed to the presence of curcumin, which contains compounds that promote cellular proliferation and contribute to cell-wall building. These positive results not only confirm the nontoxicity of the electrospun wrapper but also demonstrate its biocompatibility.

Antimicrobial materials are commonly used in food packaging to maintain food quality. Microorganisms such as *S. aureus*, *E. coli*, and fungi can proliferate in food stored for extended periods, posing significant health risks when consumed.[24–26] Among these, *S. aureus* and *E. coli* are widely known to thrive in fruit, meat, and fish. Consumption of food contaminated with these microorganisms can cause food poisoning, vomiting, and digestive disorders. Therefore, antimicrobial food packaging that can effectively inhibit *S. aureus* and *E. coli* is

© 2025 Wiley-VCH GmbH

16136829, 2025, 38, Downloaded from https://onlinelibrary.wiley.com/doi/10.1002/smll.202501808 by Korea University Library, Wiley Online Library on [28/09/2025]. See the Terms and Conditions (https://onlinelibrary.wiley.com/terms-and-conditions) on Wiley Online Library for rules of use; OA articles are governed by the applicable Creative Commons License

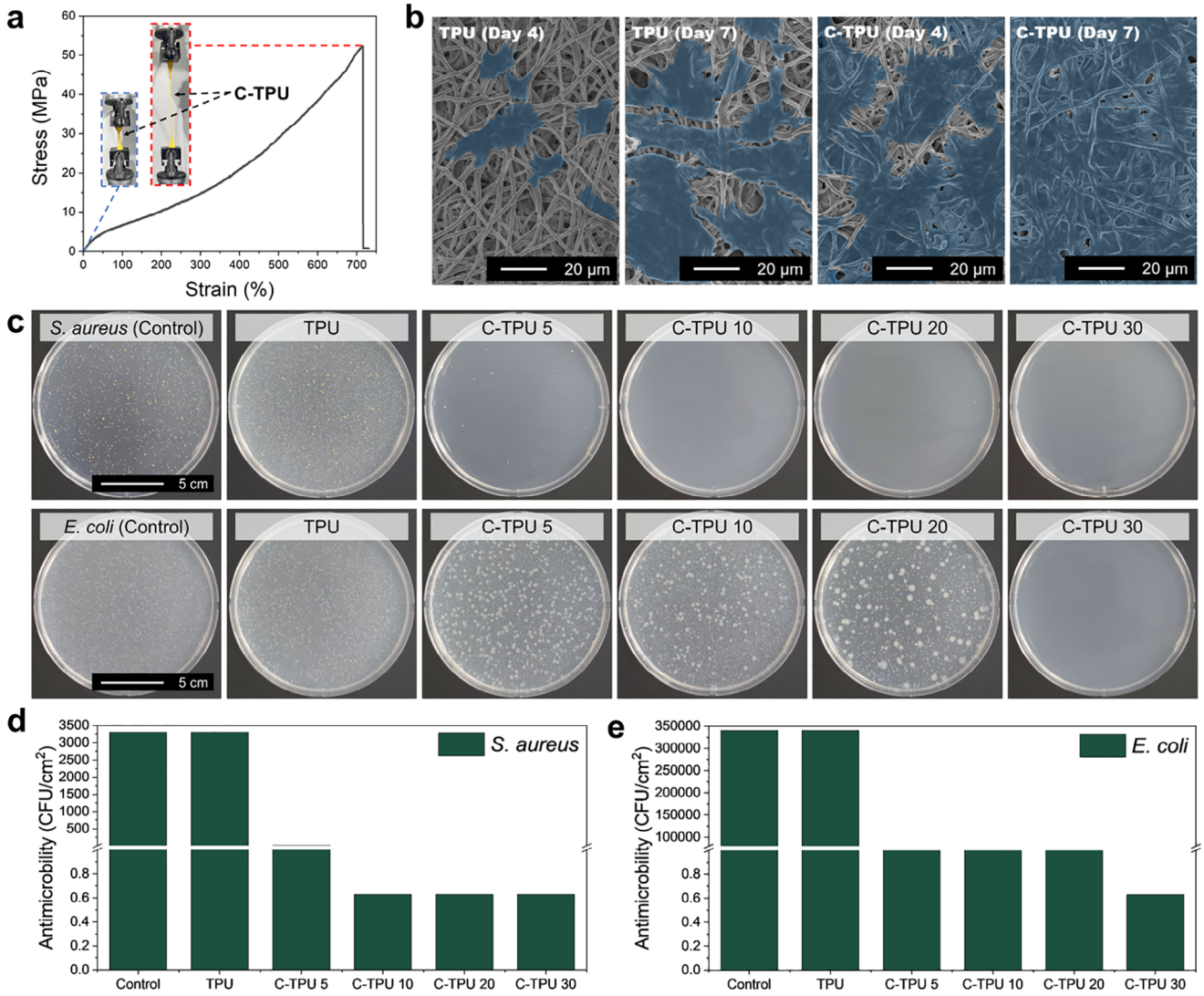


Figure 3. Characterization of the electrospun C-TPU wrapper. a) Mechanical properties of electrospun C-TPU and electrospun C-TPU with Au nanostructure arrays. C-TPU exhibits a maximum stress of 52.3 MPa, with a maximum strain of 707%. Young's modulus of C-TPU is 0.105 MPa. b) Results of the cell proliferation test to verify the biocompatibility of electrospun TPU and C-TPU. SEM images show the electrospun fibers before cell proliferation, along with cell proliferation (indicated in blue) on Days 4 and 7. c) Antimicrobial results of electrospun TPU and electrospun C-TPU with varying curcumin contents (5, 10, 20, and 30 wt.%) against *S. aureus* and *E. coli*. Antimicrobial properties were evaluated using the JIS Z 2801 test method. d) Antimicrobial properties against *S. aureus*. e) Antimicrobial properties against *E. coli*.

essential. Electrospun pure TPU wrappers do not possess inherent antimicrobial properties, leading to the active growth and distribution of *S. aureus* and *E. coli* on their surfaces, as shown in Figure 3d,e. In contrast, electrospun C-TPU exhibits enhanced antimicrobial properties due to its high polyphenol content from curcumin.[27,28] As the curcumin content increased from 5 wt.% to 30 wt.%, the antimicrobial performance of the C-TPU wrapper also improved, correlating with the increased polyphenol content. Specifically, electrospun C-TPU 30, containing 30 wt.% curcumin, demonstrated 99.99% and 99.9% antibacterial activities against *S. aureus* and *E. coli*, respectively. These fiber-based wrappers, enhanced with specialized functionalities such as stretchability, biocompatibility, and antimicrobial properties through electrospinning, are expected to significantly extend the shelf life of food by preserving its quality over longer periods.

2.4. Simulation, Optimization, and Experimental Validation of the NSSAW Metallic Nanogap as a SERS Hotspot

In molecular diagnostics and analytical chemistry, the demand for highly sensitive detection and analysis of small molecules is steadily increasing.[29] SERS, which exploits the localized surface plasmon resonance of metallic nanostructures, has garnered significant attention owing to its high specificity and sensitivity toward small molecules. These attributes enable real-time, nondestructive, and highly sensitive monitoring of food quality and

© 2025 Wiley-VCH GmbH

16136829, 2025, 38, Downloaded from https://onlinelibrary.wiley.com/doi/10.1002/smll.202501808 by Korea University Library, Wiley Online Library on [28/09/2025]. See the Terms and Conditions (https://onlinelibrary.wiley.com/terms-and-conditions) on Wiley Online Library for rules of use; OA articles are governed by the applicable Creative Commons License

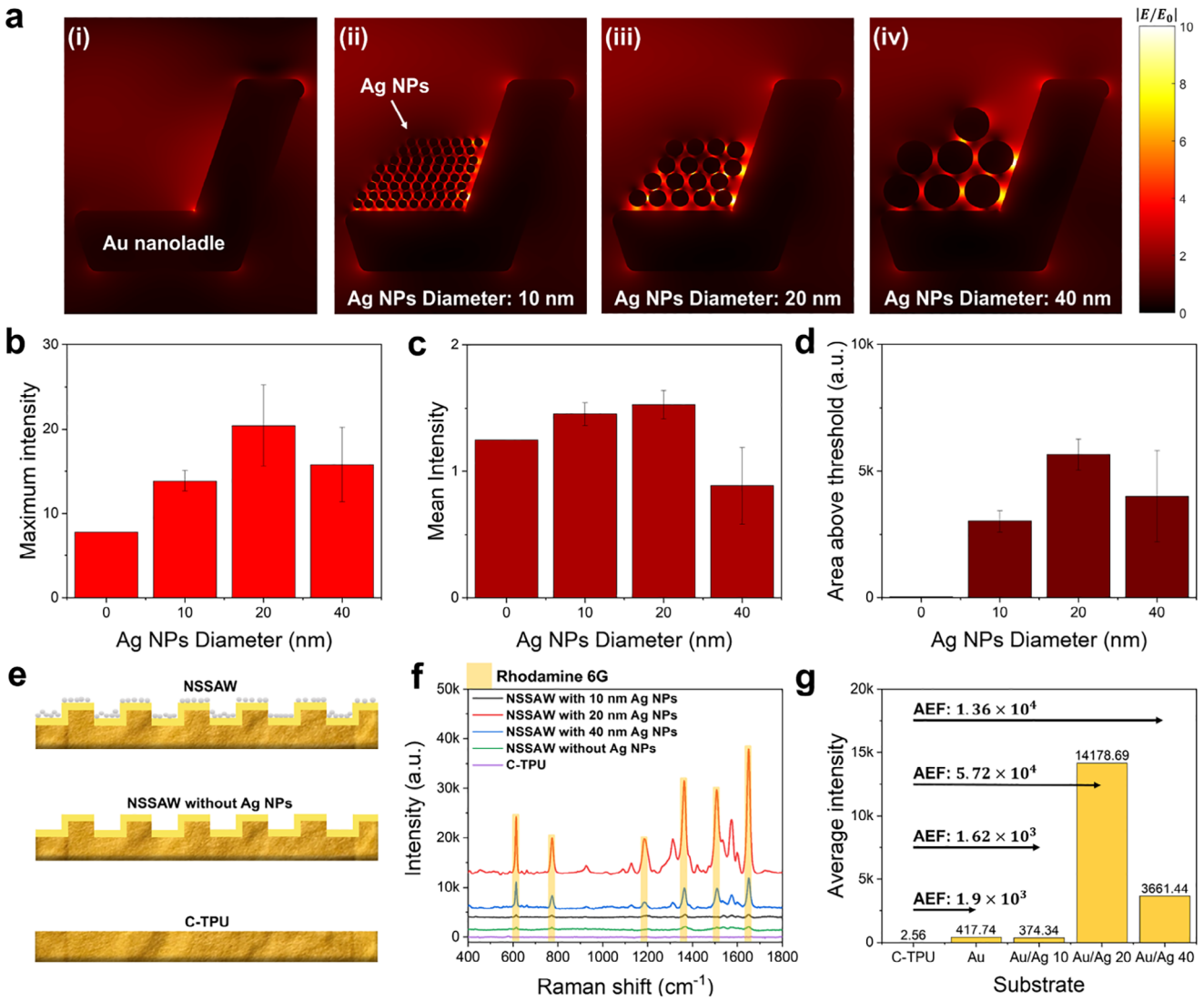


Figure 4. Electric field distribution, Ag NP diameter optimization via FDTD simulation, and performance characterization of the NSSAW metallic nanogap as an SERS hotspot. a) Visualizations of the electric field distributions for (i) the Au nanostructure without Ag NPs and (ii)–(iv) the Au nanostructure with Ag NPs of diameters 10, 20, and 40 nm, respectively. b) Maximum electric field intensity as a function of nanoparticle diameter, derived from ten simulations with randomly varied Ag NP positions. c) Average electric field intensity for each particle diameter calculated from repeated simulations. d) Area of regions where the electric field intensity exceeded the threshold value (TH = 5 V m^{-1}). The results in a-d are based on ten independent simulations for each nanoparticle diameter, with randomized Ag NP positions in each iteration. e) Performance and characterization of the developed metallic nanogap of the NSSAW as a SERS hotspot. Schematic of substrates used for evaluating Raman signal detection performance. f) Raman spectra of R6G 10^{-4} M measured for each substrate. g) Average intensity and enhancement factor corresponding to the representative R6G Raman peaks.

safety.[30] In this study, the NSSAW was designed to create numerous SERS hotspots by drop-casting a solution containing Ag NPs with diameters of 10, 20, and 40 nm onto an Au nanostructure array.

To investigate the field-enhancement effects of the Ag-embedded Au nanostructure, we conducted comprehensive FDTD simulations. This analysis aimed to optimize the size of the Ag NPs to achieve maximum localized electric field intensity and enhance the overall SERS performance of the developed sensor. The Au nanostructures, which were modeled based on their fabricated dimensions, served as the foundational geometry in the simulations. Ag NPs with diameters of 10, 20, and 40 nm were strategically positioned on the Au nanostructure disks to evaluate their influence on electromagnetic field enhancement. Plane-wave excitation at 532 nm was used to determine the optimal nanoparticle size. Simulations revealed a significant electromagnetic field enhancement near the Ag NPs. **Figure** 4a–i shows the electric field distribution for the Au nanostructure without Ag NPs, which exhibited relatively low intensities. In contrast, Figure 4a-ii–iv show the normalized electric field intensity distributions for various Ag NP diameters, highlighting substantial enhancement at the interfaces between the Au nanostructures and Ag NPs, as well as between adjacent Ag NPs. These regions of strong plasmonic coupling generated the highest field

© 2025 Wiley-VCH GmbH

16136829, 2025, 38, Downloaded from https://onlinelibrary.wiley.com/doi/10.1002/smll.202501808 by Korea University Library, Wiley Online Library on [28/09/2025]. See the Terms and Conditions (https://onlinelibrary.wiley.com/terms-and-conditions) on Wiley Online Library for rules of use; OA articles are governed by the applicable Creative Commons License

intensities, underscoring the critical role of Ag NP placement and size in optimizing the performance.

To quantitatively assess and compare the performance of each configuration, three key metrics were extracted from the simulation results: 1) maximum electric field intensity, 2) average field intensity within a defined region of interest, and 3) the area where the field intensity exceeded a threshold value (TH = 5 V m^{-1}). These metrics were selected to comprehensively evaluate the SERS performance by addressing both localized and spatially distributed effects. Calculations were performed using data from 10 independent simulations for each Ag NP configuration, with randomly varied positions to account for system variability (Figure 4b–d).[31] Figure 4b shows that the maximum electric field intensity, critical for enhancing Raman signals, is lowest for the Au nanostructures without Ag NPs, confirming that Ag NPs amplify the field through plasmonic coupling.[32,33] Among the tested sizes, the 20 nm Ag NPs exhibited the highest normalized field enhancement, with an intensity of 21.1(±5.1) compared to 13.5(±1.3) for 10 nm and 16.8(±4.7) for 40 nm particles. Figure 4c illustrates the average electric field intensity within a defined region of interest, which is defined as the proximity to the Ag NP. This metric captures the overall enhancement effect across a practical interaction volume rather than focusing solely on isolated hotspots.[34] Figure 4d quantifies the spatial extent of field enhancement, indicating the likelihood of interactions with Raman-active molecules and the resulting SERS signal intensities.[35]

Optimally sized Ag NPs effectively concentrate the electric field, inducing strong local field enhancement that amplifies SERS signals.[33] However, smaller Ag NPs (e.g., 10 nm) experience increased plasmon resonance damping due to surface scattering, which broadens the resonance peak and weakens the field enhancement.[36] In contrast, larger Ag NPs (e.g., 40 nm) exhibit dispersed electric fields and reduced intensities due to multipolar resonance effects. Among the tested sizes, 20 nm Ag NPs demonstrated superior performance across all three evaluation metrics: maximum electric field intensity, average field intensity, and the area exceeding the threshold value (TH = 5 V m^{-1}). This size was identified as optimal for maximizing the SERS enhancement under the experimental conditions. Additionally, although 30 nm Ag NPs were not used in the actual NSSAW fabrication, an additional simulation was performed to evaluate their performance. As shown in Supplementary Figure S2 (Supporting Information), the results revealed that 30 nm Ag NPs exhibited stable average intensities and a large area exceeding the threshold, highlighting their potential as an alternative for enhancing SERS signals. It is important to note, however, that the optimal Ag NP size for SERS enhancement is strongly dependent on the excitation wavelength, which dictates the localized surface plasmon resonance conditions.[32]

To compare the simulation results, the SERS hotspot performance was evaluated using Rhodamine 6G (R6G). Figure 4e presents schematic cross-sectional illustrations of the substrates used for the measurements, including a C-TPU substrate, an Au nanostructure array covered with electrospun C-TPU, and the NSSAW, which consists of Ag NPs deposited onto the Au nanostructure array on electrospun C-TPU. Figure 4f shows the Raman spectra of R6G obtained from each substrate.[37] The C-TPU substrate exhibits virtually no identifiable Raman peaks. In contrast, the NSSAWs without Ag NPs and those fabricated using a 10 nm Ag NP solution show weak signals for the major peaks, owing to the structural characteristics of the NSSAW. As shown in Figure 2k, the gaps between the Au nanostructures are ≈15 nm. From the SEM analysis shown in Supplementary Figure S3a (Supporting Information), the average diameter of the 10 nm Ag NPs solution was determined to be 14.84 nm. Consequently, using this solution resulted in most of the Ag NPs escaping through the gaps, leading to no significant performance difference compared to using only the Au nanostructure array.

Meanwhile, the NSSAW produced with a 40 nm Ag NP solution clearly displays the major Raman peaks of R6G, whereas the NSSAW fabricated with a 20 nm Ag NP solution reveals most of the R6G Raman peaks with high intensity. This improvement is attributed to the high SERS performance of Ag, the numerous SERS hotspots created by the Ag NPs, and the optimal Ag NP diameter, which was confirmed through simulation. As shown in Supplementary Figure S3b (Supporting Information), the actual diameter distribution of the 20 nm Ag NP solution revealed an average diameter of 27.4 nm, which closely aligns with the optimal diameters of 20 and 30 nm for Ag NPs, as confirmed through FDTD simulations.

Figure 4f shows a quantitative comparison of the detection sensitivities of the Raman signals obtained from each substrate. The average intensities at 614, 774, 1185, 1362, 1507, and 1650 cm^{-1}, as indicated in Figure 4e, were calculated, and the Average Enhancement Factor (AEF) was also determined. This factor represents the degree of signal amplification by the nanostructures compared with that of the R6G film and is defined as

$$\mathrm{AEF} = \left(I_{SERS}/N_{SERS}\right) \times \left(N_{Film}/I_{Film}\right) \quad (1)$$

where I_{SERS} is the SERS signal intensity, N_{SERS} is the areal density of the target molecules on the SERS substrate, N_{Film} is the areal density of the R6G film on the C-TPU, and I_{Film} is the Raman signal intensity of the R6G film. Detailed information on the AEF calculation can be found in the study by Le Ru, Eric C., et al.[38] Consequently, the AEF value for the C-TPU integrated with only the Au nanostructure array was determined to be 1.9×10^3. When the NSSAW was further coated with Ag NP solutions of 10, 20, and 40 nm, the AEF values were 1.62×10^3, 5.72×10^4, and 1.36×10^4, respectively. The introduction of 20 nm Ag NPs resulted in a significant performance enhancement, showing a 30.11-fold increase compared to the NSSAW without Ag NPs.

2.5. SERS Applications for Food Quality and Safety Assessment Using NSSAW

Monitoring freshness, nutritional content, and toxicants in food is essential for ensuring consumer health and safety. Consequently, active research is underway that utilizes advanced non-destructive analytical techniques to assess food quality and safety. The food-monitoring patch, which contains numerous SERS hot spots, enables non-destructive SERS-based analysis of food freshness and nutritional content.

First, the nutritional content of the food was analyzed using NSSAW. Ensuring accurate nutritional data is vital not only for

© 2025 Wiley-VCH GmbH

16136829, 2025, 38, Downloaded from https://onlinelibrary.wiley.com/doi/10.1002/smll.202501808 by Korea University Library, Wiley Online Library on [28/09/2025]. See the Terms and Conditions (https://onlinelibrary.wiley.com/terms-and-conditions) on Wiley Online Library for rules of use; OA articles are governed by the applicable Creative Commons License

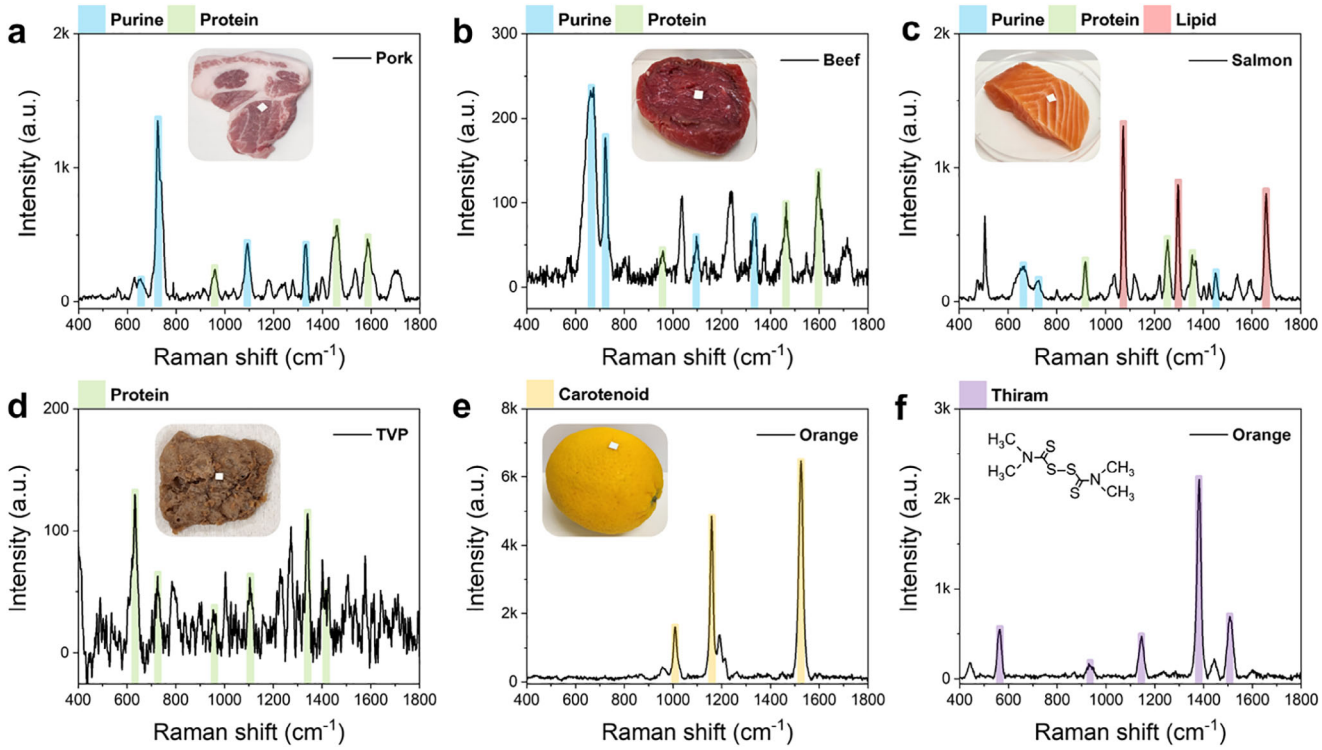


Figure 5. SERS spectra collected using NSSAW from a) pork, b) beef, c) salmon, d) TVP, e) carotenoid in orange peel, and f) thiram (10^{-4} M) applied to orange peel. Panels a–d show the characteristic peaks for purines (blue), proteins (green), and lipids (red) commonly found in food. Specifically, pork and beef display peaks for guanine (660 cm^{-1}), adenine (724 and 1333 cm^{-1}), hypoxanthine (724 and 1094 cm^{-1}), lysine (957 and 1464 cm^{-1}), and myoglobin (1585 cm^{-1}). Salmon exhibits guanine (660 cm^{-1}), adenine (724 cm^{-1}), hypoxanthine (724 and 1449 cm^{-1}), glutamic acid (917, 1254, and 1355 cm^{-1}), and fatty acids (e.g., palmitic and oleic acids) (1071, 1296, and 1656 cm^{-1}). TVP features leucine (962 and 1342 cm^{-1}) and glutamine (1103 cm^{-1}). Panel e shows β-carotene (yellow) in the orange peel, with notable peaks at 1010, 1158, and 1525 cm^{-1}. Panel f confirms the presence of the fungicide thiram (purple) at distinct peaks around 562, 933, 1145, 1382, and 1508 cm^{-1}.

nutrition professionals but also for the public to establish healthier eating habits and promote public safety.[39] In this study, SERS measurements were conducted on globally consumed foods, such as pork (**Figure 5**a), beef (Figure 5b), and salmon (Figure 5c), using NSSAW to gather nutritional information. Adenine, guanine, and hypoxanthine are purine derivatives found in pork, beef, and salmon, respectively. These compounds, particularly hypoxanthine, are metabolized into uric acid in the human body. Consuming foods with high total purine content, especially those with a high ratio of hypoxanthine, is considered a significant risk factor for hyperuricemia and related diseases such as gout.[39] In Figure 5a–c, the peaks at 726, 1094, and 1449 cm^{-1} are associated with hypoxanthine, which is directly linked to the development of gout.[40–42] Conversely, the peaks at 660 and 1333 cm^{-1} correspond to guanine and adenine, respectively, which are relatively less influential in the development of gout due to their lower contribution to uric acid formation compared to hypoxanthine.[40,42,43]

These animal and fish meats also contain high levels of proteins. In the case of pork and beef (Figure 5a,b), the peaks at 1464 and 957 cm^{-1} are associated with lysine, an essential amino acid crucial for protein synthesis and tissue repair.[44] The peak observed around 1585 cm^{-1} is attributed to myoglobin, a protein that plays a vital role in oxygen storage within muscle tissues, contributing to the red color and functionality of muscle fibers in these meats.[45] In salmon, a high proportion of glutamic acid is found in the amino acid composition of salmon protein hydrolysates.[46] In Figure 5c, the peaks at 917, 1254, and 1355 cm^{-1} are associated with glutamic acid.[44] Additionally, in salmon, SERS peaks related to fatty acids have been observed, with peaks at 1072 and 1656 cm^{-1} indicating a high proportion of palmitic acid (a saturated fat) and oleic acid (an omega-9 monounsaturated fat), respectively. The peak at 1296 cm^{-1} is attributed to both palmitic and oleic acids.[47]

For pork and beef, in addition to the previously mentioned peaks, peaks were also observed at various unidentified locations, such as 1034, 1240, and 1376 cm^{-1}. Although the intensities of these peaks vary, their positions remain consistent. Based on these observations, it can be inferred that while the compositional elements of pork and beef are nearly identical, differences exist in their proportional compositions.

Furthermore, the SERS analysis was extended to textured vegetable protein (TVP) to identify the differences in nutrient content between plant-based and animal meats. With the rapid increase in global population, protein availability has gradually become insufficient. Plant-based meat alternatives are being developed as a solution to this issue.[48] Therefore, comparing and analyzing the nutritional differences between TVP, which is gaining attention as an alternative protein source, and animal meat is important. Minimally processed soybean products are

© 2025 Wiley-VCH GmbH

16136829, 2025, 38, Downloaded from https://onlinelibrary.wiley.com/doi/10.1002/smll.202501808 by Korea University Library, Wiley Online Library on [28/09/2025]. See the Terms and Conditions (https://onlinelibrary.wiley.com/terms-and-conditions) on Wiley Online Library for rules of use; OA articles are governed by the applicable Creative Commons License

recommended for managing gout and hyperuricemia, as well as for reducing the risk of cardiovascular diseases, due to their significantly lower proportion of hypoxanthine compared to animal meats.[40] In Figure 5d, which shows the spectra of TVP, no peaks corresponding to hypoxanthine, such as those at 1094 and 1449 cm^{-1}, were observed. However, SERS peaks corresponding to amino acids like leucine and glutamine, which are present in higher proportions in soy compared to animal meat, were detected.[46] The peaks observed at 630, 725, and 1410 cm^{-1} are common in most amino acids. The peaks at 962 and 1342 cm^{-1} are attributed to leucine, while the peak at 1103 cm^{-1} is attributed to glutamine.[44] This analysis enabled a comparison of the nutritional composition of plant-based and animal meats.

Second, it has been demonstrated that NSSAW can assess the quality of fruits by identifying their compositional elements. As citrus fruits mature to higher quality, the β-carotene content in the peel, which imparts an orange color, increases compared to unripe fruits.[49] Therefore, the ability of NSSAW to detect β-carotene in citrus fruits was examined. To detect β-carotene, NSSAW was placed on the clean surface of the orange peel, and SERS analysis was conducted. As shown in Figure 5e, SERS peaks observed at approximately 1010, 1158, and 1525 cm^{-1} are indicative of the presence of β-carotene.[50] These results suggest the potential to determine the concentration of β-carotene through variations in Raman signal intensity.

Third, it has been demonstrated that NSSAW can assess both the quality and safety of citrus fruits, demonstrating its dual applicability by leveraging the characteristics of SERS technology. Thiram is a fungicide widely used to prevent crop damage and preserve harvested crops (fruits and vegetables) during storage or transportation. However, thiram residues remaining on food can cause serious health issues, including respiratory irritation, immune suppression, and effects on blood and circulation.[51] In this study, to test the applicability of NSSAW to detect thiram, thiram (10^{-4} M) was applied to the orange peel, and NSSAW was placed on top for SERS analysis. As shown in Figure 5f, SERS peaks observed around 562, 933, 1145, 1382, and 1508 cm^{-1} are indicative of the presence of thiram.[52] In conclusion, the versatility of SERS in analyzing multiple components demonstrates that NSSAW can effectively and non-destructively detect the freshness, safety, and nutritional content of food in real-time.

Finally, the functionality of NSSAW in estimating the concentration of food components via SERS measurements was examined. An analysis targeting hypoxanthine—a gout-inducing component evident in pork, beef, and salmon—was conducted. As shown in Figure S4 (Supporting Information), an increase in hypoxanthine concentration enhanced the intensity of the Raman peaks. Figure S4a (Supporting Information) illustrates the changes in the Raman spectra as a function of hypoxanthine molar concentration. Peaks were observed at Raman shift positions of 724, 1094, and 1449 cm^{-1}, corresponding to those identified in the Raman spectra of pork, beef, and salmon, respectively. Figure S4b (Supporting Information) shows that the intensities of these major peaks increased with increasing concentration. This suggests that SERS measurements can be used to estimate multiple components in foods, including hypoxanthine.

2.6. Temporal SERS Analysis of Food Freshness Using NSSAW

Fruits and meats spoil primarily due to microbial activity, which can occur during both distribution and consumer storage.[53] Thus, continuously monitoring potential food safety risks throughout the entire food supply chain is essential for ensuring consumer safety. NSSAW has been employed for the ongoing monitoring of food, assessing changes in nutritional content and safety, and confirming its preservation effects through antimicrobial properties.

First, decaying pork was monitored to evaluate NSSAW's efficacy in assessing meat safety. **Figure** 6a-i shows a photograph of pork stored at 3 °C for 16 d, with SERS measurements taken at three points marked with blue circles. It is known that bacteria, such as Clostridium spp., in decaying meat grow by metabolizing amino acids, emitting metabolites like DMDS.[54–56] Meat spoilage occurs as bacteria degrade amino acids, and the freshness of the meat can be assessed by the number of bacteria present.[57] Figure 6a-ii displays the SERS spectra of the pork over time. Compared to Day 1, the intensities of all amino acid and purine spectra significantly decreased by Day 4 and continued to decrease until Day 16. Within the 600–700 cm^{-1} range, the peak at 660 cm^{-1}, attributed to guanine, was present on Days 1 and 4. However, from Day 7 onward, the main peak at 680 cm^{-1}, indicative of DMDS, began to emerge prominently.[58] By Day 13, the intensity of the DMDS peak (680 cm^{-1}) increased, and peaks from other components were nearly undetectable. On Day 16, only the distinct DMDS peaks at 680, 950, and 1305 cm^{-1} were observed. Figure 6a-iii shows the temporal changes in hypoxanthine (724 cm^{-1}) and lysine (1464 cm^{-1}), with their intensities relative to that on Day 1, demonstrating a significant decrease over time. In contrast, the intensity of DMDS (680 cm^{-1}), relative to its value on Day 16, increased as the experiment progressed. This pattern suggests an increase in the bacterial population in pork over time.

Furthermore, it has been previously confirmed that β-carotene can be detected in orange peels using NSSAW. Moreover, it has been established that quality changes can be monitored by periodically measuring orange peels. Similar to other products, citrus fruits can suffer from bruising or diseases during handling and storage. In particular, damage caused by mold or bacterial infection can spread to other fruits, and visible signs of decay on the fruit surface may lead to increased consumer rejection of less fresh products. Additionally, it is known that as stored fruits decay and lose freshness, their β-carotene content decreases.[59] Therefore, this study explored whether changes in the SERS peak intensities of β-carotene—monitored through periodic SERS analyses of orange peels using NSSAW—can indirectly assess the freshness of oranges.

As shown in Figure 6b-i, a photograph captures the changes in the orange peel as it decays over time from storage at room temperature. The SERS measurements were focused continuously on a single point, marked by the blue circle in Figure 6b-i. Measurements were conducted at six-day intervals over a total of 19 d, with three SERS spectra obtained per measurement day. Figure 6b-ii presents the temporal β-carotene SERS spectra. A clear decrease in β-carotene intensity was observed in the orange peel. In Figure 6b-iii, the SERS peak intensity of β-carotene over time is shown relative to Day 1, clearly demonstrating a

© 2025 Wiley-VCH GmbH

16136829, 2025, 38, Downloaded from https://onlinelibrary.wiley.com/doi/10.1002/smll.202501808 by Korea University Library, Wiley Online Library on [28/09/2025]. See the Terms and Conditions (https://onlinelibrary.wiley.com/terms-and-conditions) on Wiley Online Library for rules of use; OA articles are governed by the applicable Creative Commons License

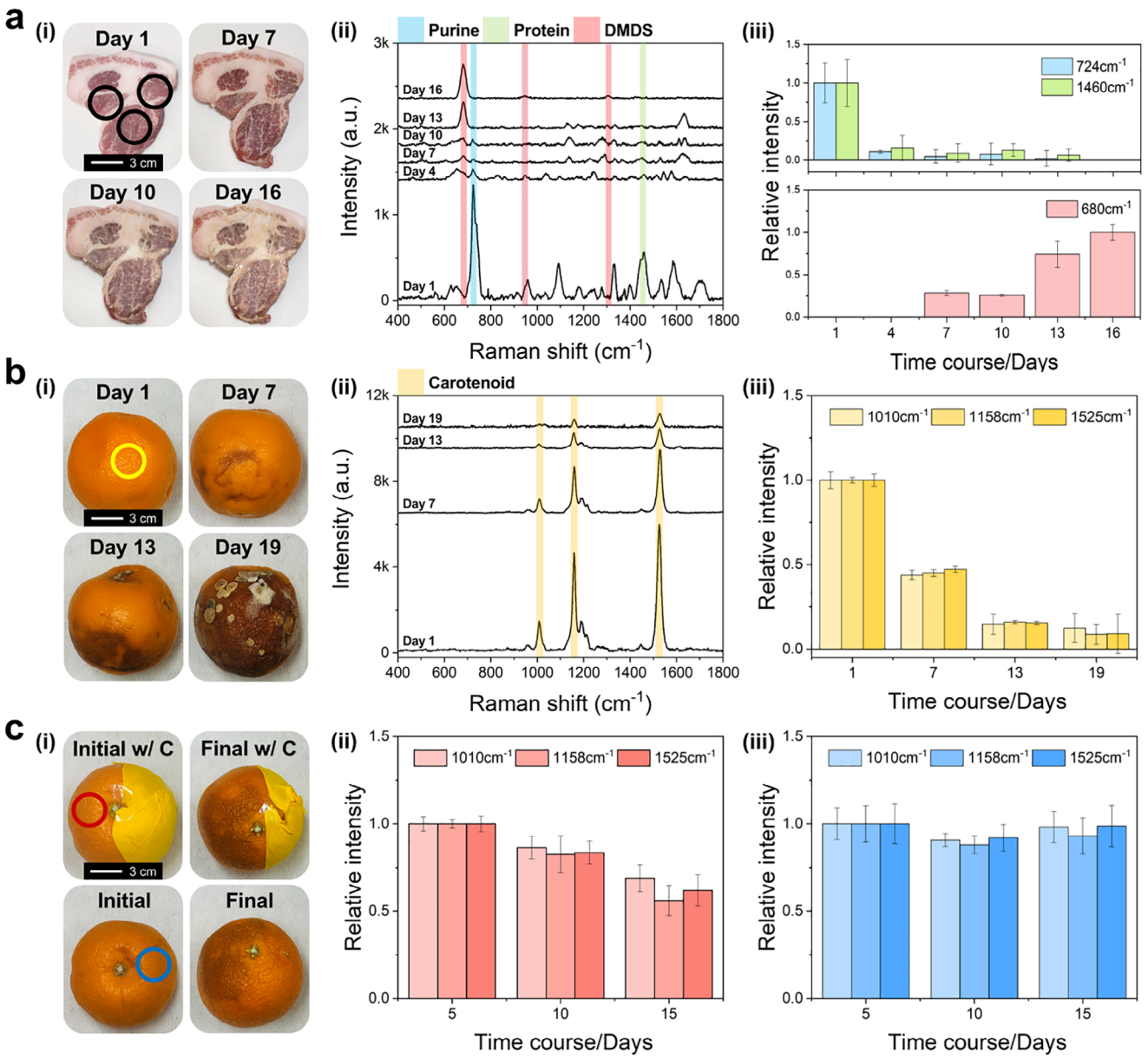


Figure 6. Temporal SERS analysis for food quality monitoring using NSSAW. a) Monitoring pork freshness. i) Photographs illustrating changes in the condition of pork over time. Measurements were taken once from three spots marked in black. ii) SERS spectra of pork collected at 3-day intervals. iii) Temporal variations in relative Raman signal intensities of purines, proteins, and DMDS in pork. b) Monitoring the freshness of oranges. i) Photographs showing changes in the oranges over time. Measurements were performed three times at the spots highlighted in yellow. ii) SERS spectra of carotenoids in orange peels collected at 6-day intervals. iii) Temporal changes in the relative Raman signal intensities of carotenoids in the orange peels. c) Verification of the antimicrobial effects of C-TPU on orange preservation. i) Photographs of oranges partially wrapped with C-TPU taken on the first and last days of the storage period. Measurements were performed three times at the spots marked in red and blue. ii) Temporal variations in the relative Raman signal intensities of carotenoids in unwrapped areas and iii) areas wrapped with C-TPU.

decreasing trend in intensity. By Day 7, it had decreased to 45% of Day 1's intensity, 15% by Day 13, and further to 10% by Day 19. Consequently, as the bright orange hue of the peel faded, a corresponding decrease in the SERS peak intensity of β-carotene was observed.

Finally, the antimicrobial properties of C-TPU were verified (Figure 6c). An orange was half-wrapped with C-TPU and stored at room temperature for 15 d. The effects of C-TPU were visually evident and confirmed by SERS measurements. As shown in Figure 6c-i, the part of the orange not covered by C-TPU underwent decay and lost its orange color, whereas the C-TPU-wrapped section of the peel showed no significant change from Day 1 to Day 15. The SERS peak intensities of β-carotene were measured separately for these two sections and compared. The measurements focused on the areas marked by the blue circle in Figure 6c-i, with three SERS spectra obtained per measurement

© 2025 Wiley-VCH GmbH

16136829, 2025, 38, Downloaded from https://onlinelibrary.wiley.com/doi/10.1002/smll.202501808 by Korea University Library, Wiley Online Library on [28/09/2025]. See the Terms and Conditions (https://onlinelibrary.wiley.com/terms-and-conditions) on Wiley Online Library for rules of use; OA articles are governed by the applicable Creative Commons License

day. Figure 6c-ii displays the relative SERS peak intensity of the orange peel without C-TPU, based on Day 1. On average, the intensity decreased to 84% on Day 1 by Day 8 and to 62% by Day 15. Conversely, Figure 6c-iii shows the SERS peak intensity of the orange peel with C-TPU, which remained stable at 90% on Day 1 on Day 8 and 96% on Day 15. In addition to its monitoring capabilities, these experiments demonstrated that C-TPU effectively inhibited microbial decay, facilitating long-term food preservation. NSSAW distinguishes itself from conventional sensors by preserving food quality while enabling the monitoring of multiple components. As shown in Table S1 (Supporting Information), although its sensitivity (AEF) is lower than that of traditional food-monitoring sensors, it can still clearly detect various components, and its flexible elastic substrate provides a practical format ideally suited for food monitoring.

3. Conclusion

This study introduces the development of NSSAW as an innovative solution for real-time, non-destructive food quality monitoring and as a stretchable, antimicrobial wrapper for food preservation. The NSSAW system integrates advanced fabrication techniques, including NIL, nTP, and electrospinning, to create an Au nanostructure array loaded with Ag NPs. This design generates numerous SERS hotspots, significantly enhancing the Raman signal and enabling the sensitive detection of nutritional content, freshness, and toxicants in food. The incorporation of the Au nanostructure sensor into the electrospun TPU wrapper, infused with curcumin, provided remarkable elasticity and antimicrobial properties. This wrapper actively inhibits microbial growth, thereby extending the preservation period and maintaining food quality. The efficacy of the NSSAW system was confirmed by the successful detection of key food components, such as purines, proteins, and lipids in salmon, TVP, beef, and pork, as well as carotenoids and thiram in oranges. Furthermore, the system demonstrated its capability to monitor and slow spoilage progression by detecting DMDS peaks, which are markers of bacterial activity.

However, challenges remain regarding the reusability and washability of the system. Although the SERS substrate contains only nanoscale amounts of Au and Ag, the cost could be a concern if the system is employed as a disposable product. Ideally, both the wrapper and sensor components should be washable and reusable. Although acetone- and ethanol-based cleaning methods for SERS substrates are well established, these solvents may wash away the Ag NPs. Future development of substrates in which Ag NPs are more securely encapsulated by Au could significantly improve the practicality and durability of the sensor.

Another limitation is the reliability and consistency of the SERS signals and the subsequent data analysis. Although the NSSAW system demonstrated excellent sensitivity, further validation is required to ensure the robustness and reproducibility of the detected signals across different food matrices. By integrating food chemistry and microbiology approaches for a more in-depth analysis, coupled with the accumulation of large-scale datasets, the signal accuracy could be further enhanced. Additionally, incorporating AI-based classification and big data analysis would facilitate the creation of advanced predictive models, improving the system's ability to identify spoilage patterns and classify food quality with greater precision.

In conclusion, NSSAW represents a significant advancement in smart food packaging and provides a practical solution for real-time food monitoring, enhancing food safety and quality. This system holds promise for portable food monitoring and preservation, with potential applications ranging from home food quality testing to restaurants, large-scale farms, and smart-farming environments. This approach offers considerable potential for replacing traditional food packaging materials, contributing to the wellness era by ensuring safer and longer-lasting food products. Detailed information regarding the SERS peaks for all the components is provided in Supplementary Table S2 (Supporting Information).

4. Experimental Section

Materials: The PUA resin used for nanoimprinting was RM-311 (Minuta Technology Co., Ltd., Republic of Korea). The TPU film for the electrospinning process was obtained from Woojin Corporation, whereas N, N-Dimethylformamide (DMF) and ethyl acetate (EA) were purchased from Deoksan Chemical. Curcumin and a 20 nm Ag NPs solution were acquired from Sigma Aldrich.

Fabrication: Silicon (Si) master molds with a nanostructure array were fabricated using krypton fluoride lithography. The process began with photolithography, where a 58 nm-thick bottom anti-reflective coating layer and a 1.0 µm-thick photoresist layer were sequentially deposited onto the substrate. The substrate was then soft-baked at 100 °C for 60 s, followed by a post-exposure bake at 110 °C for 660 s. The substrate was then immersed in a developer solution for 60 s to remove the exposed regions of the photoresist. The etching process was conducted using a gas mixture of Cl_2 at a flow rate of 30 sccm and HBr at a flow rate of 180 sccm under a pressure of 12 mTorr and power of 300 W. This selective etching of the exposed areas of the Si substrate resulted in the desired nanopatterned Si master mold.[60–63]

The PUA-based mold was replicated from the fabricated nanostructure array master mold. PUA resin was applied to the nanopatterned Si master mold, which was then covered with a polyethylene terephthalate film and uniformly pressed with a roller. The PUA resin was cured by exposure to UV light, with a light source set to a power of 56 mW, and the curing process was performed for 3 min. Au was then deposited onto the surface of the nanostructured PUA mold using an e-beam evaporator at a deposition rate of 1.0 Å s^{-1}, resulting in a 100 nm-thick Au layer.

To improve the stability of the Au nanostructure array transfer, side etching and surface modification of the PUA molds were performed using oxygen plasma treatment for 20 min. Following plasma treatment, the Au nanostructure array was grounded, and TPU electrospinning was performed on its surface. The TPU solution was prepared by dissolving a 20 wt.% TPU film in a 1:1 mixture of DMF and EA. Curcumin was then incorporated into the TPU solution at concentrations of 5, 10, 20, and 30 wt.% relative to the mass of TPU, depending on the specific requirements. Electrospinning of TPU and curcumin-infused TPU (C-TPU) was performed at a voltage of 20 kV and a spinning rate of 1.5 mL h^{-1} for 2 h, with a 15 cm distance between the grounded substrate and the nozzle. During electrospinning, the Au nanostructure array on the grounded surface was transferred to the electrospun fibers via electrostatic attraction. The electrostatic forces generated during the electrospinning process result from electrostatic charging and dissipation between the electrospun fibers and grounded substrate. These forces play a crucial role in facilitating the transfer of Au nanostructures onto the electrospun textiles. Upon completion of the electrospinning process and detachment of the electrospun wrapper from the ground, the Au nanostructure array was successfully transferred to the surface.

Finally, a solution of Ag NPs was drop-cast onto the electrospun wrappers containing the transferred Au nanostructure array. At room

© 2025 Wiley-VCH GmbH

16136829, 2025, 38, Downloaded from https://onlinelibrary.wiley.com/doi/10.1002/smll.202501808 by Korea University Library, Wiley Online Library on [28/09/2025]. See the Terms and Conditions (https://onlinelibrary.wiley.com/terms-and-conditions) on Wiley Online Library for rules of use; OA articles are governed by the applicable Creative Commons License

temperature, the solvent was allowed to evaporate, and the Ag NPs were embedded within the Au nanostructures. The number of drop-casting cycles for the Ag NPs solution was set to five because, as shown in Figure S5 (Supporting Information), increasing the number of cycles to four significantly enhanced the Raman peak intensity, whereas beyond four cycles, the change was small. Therefore, a five-cycle process was adopted to ensure the high sensitivity and economic feasibility of Ag NPs.

Morphological Analysis and Basic Characterization: The surfaces of the specimens were examined using SEM (FEI Sirion, Japan). The electrospun fiber surfaces were similarly analyzed using SEM, and the fiber diameters were measured and classified using ImageJ software. The Au nanostructure molds were observed using AFM (Park Systems NX20 300 & FX40, Republic of Korea) and SEM. Additionally, sectioning and cross-sectional analyses were conducted using focused ion beam SEM (FIB-SEM, Hitachi FB-2100, Japan) to assess the etch rate of the PUA molds as a function of the oxygen plasma treatment time. TEM, Jeol LTD JEM-2100F HR, Japan) and energy-dispersive X-ray spectroscopy (EDS) mapping were used to examine the Au nanostructures containing Ag NPs. FTIR analysis (range: 4000–400 cm^{-1}) was performed using an FTIR spectrometer (Thermo Fisher Scientific Nicolet iS50, USA). Mechanical properties were evaluated using a universal testing machine (AGS-X, Shimadzu, Japan).

Cell Proliferation Test: To investigate the cytotoxicity of TPU and C-TPU, a WST-1 cell proliferation assay (Premix WST-1 Cell Proliferation Assay System; Takara, Japan) was performed to measure mitochondrial dehydrogenase activity. The samples were sterilized with 70% ethanol for 1 min and washed three times with phosphate-buffered saline (PBS; Hyclone, USA) to remove residual ethanol. A total of 5×10^4 cells per sterilized sample were seeded under sterile conditions and cultured for 1, 3, and 7 d in an incubator. The assay reagent was prepared by mixing the WST-1 solution with DMEM at a 10:1 ratio. For each sample, 500 µL of the reagent was added and incubated for 1 h. Subsequently, 100 µL of the reacted supernatant was transferred to a 96-well plate, and the absorbance was measured at 440 nm using a microplate reader (SpectraMax iD3; Molecular Devices, USA).

Antimicrobial Activity: The antimicrobial effectiveness of the electrospun TPU and C-TPU textiles against *E. coli* and *S. aureus* was evaluated according to the JIS Z 2801 standard protocol. A nutrient-rich agar medium (comprising 5 g Bacto-Peptone, 3 g beef extract, and 1000 mL deionized water) was prepared to cultivate the microbes. The medium was sterilized by autoclaving at 10^3 kPa and 120 °C. Bacterial cultures were grown in 10 mL of nutrient agar at 37 ± 1 °C for 24–48 h. The test was conducted by incubating three control specimens and three treated samples in a glass container for 18 h. All the culture plates were incubated at 37 ± 1 °C for 24–48 h. After incubation, colonies in Petri dishes containing 30–300 colony-forming units were enumerated. The viable microbial count (M) was determined using the following Equation (2):

$$M = Z \times R \times 20 \tag{2}$$

where Z represents the number of colonies, R is the dilution factor, and 20 corresponds to the saline volume in milliliters. The reduction in the microbial count was calculated using the following Equation (3):

$$\text{Reduction rate} = \log M_a - \log M_c \tag{3}$$

where M_a denotes the initial live microbial number in the control, and M_c denotes the live microbial number after 18 h of incubation.

FDTD Simulation: The simulations were performed using the FDTD method implemented in the commercial software ANSYS Lumerical FDTD. Unpolarized light was modeled using the total-field scattered-field method, which is well-suited for studying scattering from small particles. The dielectric constants of the materials used in the simulation were defined as $\epsilon_{Ag} = -11 + 1.6i$ for Ag and $\epsilon_{Au} = -3.6 + 1.7i$ for Au at a wavelength of 532 nm. Periodic boundary conditions were applied along the x-axis, and perfectly matched layers were used along the y-axis to eliminate reflections. A mesh refinement technique was employed to accurately model the plasmonic resonance and field enhancement at nanoparticle-structure interfaces. This technique adapts the mesh to conform to material boundaries, enhancing the field resolution and minimizing numerical artifacts while maintaining computational efficiency.

Surface-Enhanced Raman Signal Measurement: Substrates used for Raman signal measurements were prepared by drop-casting 100 µL of a 20 nm Ag NP solution onto an Au nanostructure array using a micropipette, with the process repeated five times, including drying steps between applications. For food monitoring, 0.25 cm^2 substrates were placed onto the food items. Pork, beef, salmon, TVP, and oranges were purchased from a local market, and each item was cut to a uniform size to ensure measurement consistency. R6G (56226, Sigma Aldrich, Republic of Korea), hypoxanthine (H9377, Sigma Aldrich, Republic of Korea), and thiram (45689, Sigma Aldrich, Republic of Korea) were dissolved in ethanol using a hotplate-equipped magnetic stirrer to prepare the respective solutions. A 50 µL solution was applied to 1 cm^2 substrates, followed by drying the solvent. SERS measurements were performed using a Raman spectrometer (ACRON, Confocal Micro Raman Mapping System, Uninanotech Co., Ltd., Republic of Korea), with a 532 nm laser operating at a power of 50 mW. An ND filter value of 1% was used for food and hypoxanthine measurements, whereas a 10% filter was applied for R6G measurements. All Raman signals were collected for 10 s using a grating with 1200 grooves. The spectral data were baseline-corrected using Origin software.

Supporting Information

Supporting Information is available from the Wiley Online Library or from the author.

Acknowledgements

J.-H.H. and J.Y. contributed equally to this work. This work was supported by the National Research Foundation of Korea (NRF) grant funded by the Korean government (MSIT, No. RS-2025-00523026), by the Korea Evaluation Institute of Industrial Technology (KEIT) grant funded by the Korean government (MOTIE, Grant No. RS-2022-00154781, Development of large-area wafer-level flexible/stretchable hybrid sensor platform technology for form-factor-free highly integrated convergence sensor), by the NRF Sejong Science Fellowship (NRF-2022R1C1C2009430) funded by the MSIT of the Korean government, Alchemist Project grant funded by the Korea Evaluation Institute of Industrial Technology (KEIT) & theKoreaGovernment(MOTIE) ProjectNumber:1415179744, 20019169) and Ministry of Culture, Sports and Tourism and Korea Creative Content Agency (ProjectNumber:RS-2024-00343692), by the NRF Sejong Science Fellowship (RS- 2025–00517017) funded by the MSIT of the Korean government, and by the Collabo R&D between Industry, Academy, and Research Institute (RS-2025-02311282) funded by the Ministry of SMEs and Startups (MSS, Republic of Korea).

Conflict of Interest

The authors declare no conflict of interest.

Data Availability Statement

The data that support the findings of this study are available from the corresponding author upon request.

Keywords

antimicrobial wrapper, electrospinning, food quality monitoring, nanotransfer printing (nTP), surface-enhanced Raman scattering (SERS)

Received: February 12, 2025
Revised: May 19, 2025
Published online: May 30, 2025

© 2025 Wiley-VCH GmbH

16136829, 2025, 38, Downloaded from https://onlinelibrary.wiley.com/doi/10.1002/smll.202501808 by Korea University Library, Wiley Online Library on [28/09/2025]. See the Terms and Conditions (https://onlinelibrary.wiley.com/terms-and-conditions) on Wiley Online Library for rules of use; OA articles are governed by the applicable Creative Commons License

[1] F. Gaupp, C. Ruggeri Laderchi, H. Lotze-Campen, F. DeClerck, B. L. Bodirsky, S. Lowder, A. Popp, R. Kanbur, O. Edenhofer, R. Nugent, J. Fanzo, S. Dietz, S. Nordhagen, S. Fan, *Nat. Food.* **2021**, *2*, 928.
[2] R. Ambikapathi, K. R. Schneider, B. Davis, M. Herrero, P. Winters, J. C. Fanzo, *Nat. Food.* **2022**, *3*, 764.
[3] D. Mozaffarian, N. H. El-Abbadi, M. O'Hearn, J. Erndt-Marino, W. A. Masters, P. Jacques, P. Shi, J. B. Blumberg, R. Micha, *Nat. Food.* **2021**, *2*, 809.
[4] Y. Guo, *Nat. Food.* **2021**, *2*, 138.
[5] J. Johnson, D. Atkin, K. Lee, M. Sell, S. Chandra, *Meat Sci.* **2019**, *150*, 40.
[6] A. Singh, S. Poshtiban, S. Evoy, *Sensors (Basel)*. **2013**, *13*, 1763.
[7] L. Jiang, M. M. Hassan, S. Ali, H. Li, R. Sheng, Q. Chen, *Trends Food Sci. Technol.* **2021**, *112*, 225.
[8] C. Liu, D. Xu, X. Dong, Q. Huang, *Trends Food Sci. Technol.* **2022**, *128*, 90.
[9] B. Zhou, W. Ou, C. Zhao, J. Shen, G. Zhang, X. Tang, Z. Deng, G. Zhu, Y. Y. Li, J. Lu, *Chem. Eng. J.* **2021**, *426*, 130733.
[10] A. Nilghaz, S. Mahdi Mousavi, A. Amiri, J. Tian, R. Cao, X. Wang, *J. Agric. Food Chem.* **2022**, *70*, 5463.
[11] J. Neng, Q. Zhang, P. Sun, *Biosensors and Bioeletronics.* **2020**, *167*, 112480.
[12] L. Tian, M. Su, F. Yu, Y. Xu, X. Li, L. Li, H. Liu, W. Tan, *Nat. Commun.* **2018**, *9*, 3642.
[13] C. Chen, Y. Li, S. Kerman, P. Neutens, K. Willems, S. Cornelissen, L. Lagae, T. Stakenborg, P. Van Dorpe, *Nat. Commun.* **2018**, *9*, 1733.
[14] X. Bi, D. M. Czajkowsky, Z. Shao, J. Ye, *Nature* **2024**, *628*, 771.
[15] Z. J. Zhao, J. Ahn, J. Ko, Y. Jeong, M. Bok, S. H. Hwang, H. J. Kang, S. Jeon, J. Choi, I. Park, J. H. Jeong, *ACS Appl. Mater. Interfaces.* **2021**, *13*, 3358.
[16] C. Li, Y. Zhang, Z. Ye, S. E. J. Bell, Y. Xu, *Nat. Protoc. (Springer)* **2023**, *18*, 2717.
[17] W. K. Son, Y. S. Choi, Y. W. Han, D. W. Shin, K. Min, J. Shin, M. J. Lee, H. Son, D. H. Jeong, S. Y. Kwak, *Nat. Nanotechnol.* **2023**, *18*, 205.
[18] Z. J. Zhao, J. Ahn, S. H. Hwang, J. Ko, Y. Jeong, M. Bok, H. J. Kang, J. Choi, S. Jeon, I. Park, J. H. Jeong, *ACS Nano* **2021**, *15*, 503.
[19] J. Ahn, J. H. Ha, Y. Jeong, Y. Jung, J. Choi, J. Gu, S. H. Hwang, M. Kang, J. Ko, S. Cho, H. Han, K. Kang, J. Park, S. Jeon, J. H. Jeong, I. Park, *Nat. Commun.* **2023**, *14*, 833.
[20] J. Ahn, H. Jang, Y. Jeong, S. Choi, J. Ko, S. H. Hwang, J. H. Jeong, Y. S. Jung, I. Park, *Adv. Sci. (Weinh)* **2024**, *11*, 2303704.
[21] J. Ahn, J. Gu, Y. Jeong, J. H. Ha, J. Ko, B. Kang, S. H. Hwang, J. Park, S. Jeon, H. Kim, J. H. Jeong, I. Park, *ACS Nano* **2023**, *17*, 5935.
[22] J. H. Ha, J. Ko, J. Ahn, Y. Jeong, J. Ahn, S. Hwang, S. Jeon, D. Kim, S. A. Park, J. Gu, J. Choi, H. Han, C. Han, B. Kang, B. H. Kang, S. Cho, Y. J. Kwon, C. Kim, S. Choi, G. D. Sim, J. H. Jeong, I. Park, *Adv. Funct. Mater.* **2024**, *34*, 2401404.
[23] J. H. Ha, Y. Jeong, J. Ahn, S. Hwang, S. Jeon, D. Kim, J. Ko, B. Kang, Y. Jung, J. Choi, H. Han, J. Gu, S. Cho, H. Kim, M. Bok, S. A. Park, J. H. Jeong, I. Park, *Mater. Horiz.* **2023**, *10*, 4163.
[24] R. Boss, G. Overesch, A. Baumgartner, *J. Food Prot.* **2016**, *79*, 1240.
[25] C. I. Kothe, J. P. Pessoa, P. S. Malheiros, E. C. Tondo, *J. Infect. Dev. Ctries.* **2019**, *13*, 480.
[26] J. M. Miranda, B. I. Vázquez, C. A. Fente, P. Calo-Mata, A. Cepeda, C. M. Franco, *J. Food Prot.* **2008**, *71*, 2537.
[27] S. Cho, J. H. Ha, J. Ahn, H. Han, Y. Jeong, S. Jeon, S. Hwang, J. Choi, Y. S. Oh, D. Kim, S. A. Park, D. Lee, J. Ahn, B. Kang, B. H. Kang, J. H. Jeong, I. Park, *Adv. Funct. Mater.* **2024**, *34*, 2316196.
[28] J. H. Ha, J. Y. Kim, D. Kim, J. Ahn, Y. Jeong, J. Ko, S. Hwang, S. Jeon, Y. Jung, J. Gu, H. Han, J. Choi, G. Lee, M. Bok, S. A. Park, Y. S. Cho, J. H. Jeong, I. Park, *Adv. Mater. Technol.* **2023**, *8*, 2201765.
[29] S. O. Kelley, C. A. Mirkin, D. R. Walt, R. F. Ismagilov, M. Toner, E. H. Sargent, *Nat. Nanotechnol.* **2014**, *9*, 969.
[30] B. Sharma, R. R. Frontiera, A.-I. Henry, E. Ringe, R. P. Van Duyne, *Mater. Today* **2012**, *15*, 16.
[31] B. B. Yousif, A. S. Samra, *J. Nanopart. Res.* **2013**, *15*, 1341.
[32] H. Xin, B. Namgung, L. P. Lee, *Nat. Rev. Mater.* **2018**, *3*, 228.
[33] S. Y. Ding, J. Yi, J. F. Li, B. Ren, D. Y. Wu, R. Panneerselvam, Z. Q. Tian, *Nat. Rev. Mater.* **2016**, *1*, 16021.
[34] W. L. Barnes, A. Dereux, T. W. Ebbesen, *Nature* **2003**, *424*, 824.
[35] J. Kneipp, B. Wittig, H. Bohr, K. Kneipp, *Theor. Chem. Acc.* **2010**, *125*, 319.
[36] J. Olson, S. Dominguez-Medina, A. Hoggard, L. Y. Wang, W. S. Chang, S. Link, *Chem. Soc. Rev.* **2015**, *44*, 40.
[37] F. Zhong, Z. Wu, J. Guo, D. Jia, *Nanomaterials (Basel)* **2018**, *8*, 872.
[38] E. C. Le Ru, E. Blackie, M. Meyer, P. G. Etchegoin, *J. Phys. Chem. C* **2007**, *111*, 13794.
[39] I. Elmadfa, A. L. Meyer, *Eur. J. Clin. Nutr.* **2010**, *64*, S4.
[40] K. Kaneko, Y. Aoyagi, T. Fukuuchi, K. Inazawa, N. Yamaoka, *Biol. Pharm. Bull.* **2014**, *37*, 709.
[41] P. Hu, X. S. Zheng, C. Zong, M. H. Li, L. Y. Zhang, W. Li, B. Ren, *J. Raman Spectrosc.* **2014**, *45*, 565.
[42] J. Pan, X. Shao, Y. Zhu, B. Dong, Y. Wang, X. Kang, N. Chen, Z. Chen, S. Liu, W. Xue, *Int. J. Nanomedicine.* **2019**, *14*, 431.
[43] F. Madzharova, Z. Heiner, M. Gühlke, J. Kneipp, *J. Phys. Chem. C Nanomater. Interfaces* **2016**, *120*, 15415.
[44] S. Stewart, P. M. Fredericks, *Spectrochim. Acta A* **1999**, *55*, 1641.
[45] A. Rygula, K. Majzner, K. M. Marzec, A. Kaczor, M. Pilarczyk, M. Baranska, *J. Raman Spectrosc.* **2013**, *44*, 1061.
[46] B. Caballero, P. Finglas, F. Toldrá, *Encyclopedia of Food and Health*, Academic Press, New York USA **2015**.
[47] J. De Gelder, K. De Gussem, P. Vandenabeele, L. Moens, *J. Raman Spectrosc.* **2007**, *38*, 1133.
[48] T. Zhang, W. Dou, X. Zhang, Y. Zhao, Y. Zhang, L. Jiang, X. Sui, *Trends Food Sci. Technol.* **2021**, *109*, 702.
[49] M. J. Rodrigo, B. Alquézar, E. Alós, J. Lado, L. Zacarías, *Sci. Hortic.* **2013**, *163*, 46.
[50] F. Nekvapil, I. Brezestean, D. Barchewitz, B. Glamuzina, V. Chiş, S. Cintă Pinzaru, *Food Chem.* **2018**, *242*, 560.
[51] K. Liu, Y. Li, M. Iqbal, Z. Tang, H. Zhang, *Chemosphere.* **2022**, *295*, 133928.
[52] M. B. Bhavya, R. Prabhu B, B. M. Shenoy, P. Bhol, S. Swain, M. Saxena, N. S. John, G. Hegde, A. K. Samal, *Environ. Sci. Nano.* **2020**, *7*, 3999.
[53] S. T. Hammond, J. H. Brown, J. R. Burger, T. P. Flanagan, T. S. Fristoe, N. Mercado-Silva, J. C. Nekola, J. G. Okie, *J. Bio Sci.* **2015**, *65*, 758.
[54] T. Ali, A. Sarwar, A. A. Anjum, *Animal Biosci.* **2024**, *37*, 1970.
[55] S. García, J. E. Vidal, N. Heredia, V. K. Juneja, *Food Microbiology: Fundamentals and Frontiers*, Wiley, New York **2019**, pp. 513–540.
[56] P. Biwer, M. Neumann-Schaal, P. Henke, D. Jahn, S. Schulz, *Front. microbiol.* **2022**, *13*, 864587.
[57] K. H. Erna, K. Rovina, S. Mantihal, *J. Packag, Technol. Res.* **2021**, *5*, 127.
[58] W. Wang, S. Kang, P. J. Vikesland, *Environ. Sci. Technol.* **2021**, *55*, 9119.
[59] M. I. Gil, E. Aguayo, A. A. Kader, *J. Agric. Food Chem.* **2006**, *54*, 4284.
[60] J.-H. Ha, I. Yang, J. Ahn, S. Kang, Z.-J. Zhao, Y. Jeong, H. Je, J. Cheong, S. H. Hwang, S. Jeon, J.-H. Jeong, S. Kim, I. Park, *Adv. Funct. Mater.* **2024**, *34*, 2315028.
[61] J. Ahn, S. Padmajan Sasikala, Y. Jeong, J. G. Kim, J. H. Ha, S. H. Hwang, S. Jeon, J. Choi, B. H. Kang, J. Ahn, J. H. Jeong, S. O. Kim, I. Park, *Adv. Fiber Mater.* **2024**, *6*, 1927.
[62] J. Ahn, Y. Jeong, M. Kang, J. Ahn, S. Padmajan Sasikala, I. Yang, J. H. Ha, S. H. Hwang, S. Jeon, J. Gu, J. Choi, B. H. Kang, S. O. Kim, S. Kim, J. Choi, J. H. Jeong, I. Park, *Small.* **2024**, *20*, 2311736.
[63] H. Jang, J. Ahn, Y. Jeong, J. H. Ha, J. H. Jeong, M. W. Oh, I. Park, Y. S. Jung, *Adv. Mater.* **2024**, *36*, 2408320.

© 2025 Wiley-VCH GmbH

16136829, 2025, 38, Downloaded from https://onlinelibrary.wiley.com/doi/10.1002/smll.202501808 by Korea University Library, Wiley Online Library on [28/09/2025]. See the Terms and Conditions (https://onlinelibrary.wiley.com/terms-and-conditions) on Wiley Online Library for rules of use; OA articles are governed by the applicable Creative Commons License